Lattice dynamics and thermal transport in multiferroic CuCrO_{2}

Dipanshu Bansal, Jennifer L. Niedziela, Andrew F. May, Ayman Said, Georg Ehlers, Douglas L. Abernathy, Ashfia Huq, Melanie Kirkham, Haidong Zhou, and Olivier Delaire

Phys. Rev. B **95**, 054306 — Published 9 February 2017

DOI: 10.1103/PhysRevB.95.054306

Lattice dynamics and thermal transport in multiferroic $CuCrO_2$

Dipanshu Bansal,* Jennifer L. Niedziela, and Andrew F. May
Materials Science and Technology Division, Oak Ridge National Laboratory, Oak Ridge, Tennessee 37831, USA

Ayman Said
Advanced Photon Source, Argonne National Laboratory, Argonne, Illinois 60439, USA

Georg Ehlers and Douglas L. Abernathy
Quantum Condensed Matter Division, Oak Ridge National Laboratory, Oak Ridge, Tennessee 37831, USA

Ashfia Huq and Melanie Kirkham
Chemical and Engineering Materials Division, Oak Ridge National Laboratory, Oak Ridge, Tennessee 37831, USA

Haidong Zhou
Department of Physics and Astronomy, University of Tennessee, Knoxville, Tennessee 37996, USA

Olivier Delaire†
Mechanical Engineering and Materials Science, Duke University, Durham, North Carolina 27708, USA and
Materials Science and Technology Division, Oak Ridge National Laboratory, Oak Ridge, Tennessee 37831, USA

(Dated: January 23, 2017)

Inelastic neutron and x-ray scattering measurements of phonons and spin waves were performed in the delafossite compound $CuCrO_2$ over a wide range of temperature, and complemented with first-principles lattice dynamics simulations. The phonon dispersions and density of states are well reproduced by our density functional calculations, and reveal a strong anisotropy of Cu vibrations, which exhibit low-frequency modes of large amplitude parallel to the basal plane of the layered delafossite structure. The low frequency in-plane modes also show a systematic temperature dependence of neutron and x-ray scattering intensities. In addition, we find that spin fluctuations persist above 300 K, far above the Néel temperature for long-range antiferromagnetic order, $T_N \simeq 24$ K. Our modeling of the thermal conductivity, based on our phonon measurements and simulations, reveals a significant anisotropy and indicates that spin fluctuations above T_N constitute an important source of phonon scattering, considerably suppressing the thermal conductivity compared to that of the isostructural but non-magnetic compound $CuAlO_2$.

PACS numbers: 63.20.D-, 63.20.kk, 63.20.dk, 66.70.-f, 75.30.Ds

I. INTRODUCTION

Couplings between lattice and electronic or spin degrees of freedom underpin a wide range of material phenomena, including superconductivity, thermoelectricity, and multiferroicity. Multiferroics display both magnetic ordering and ferroelectric behavior, potentially enabling a useful two-way manipulation of magnetic or ferroelectric orders through their interaction. In many multiferroics, the magnetic and ferroelectric transition temperatures are well separated. For example, $YMnO_3$ undergoes a ferroelectric transition at ~1260 K [1], while its Néel temperature is $T_N \simeq 75$ K [2]. In such multiferroics, the coupling between the two orders may be expected to be weak, or at least indirect, as two separate underlying mechanisms drive the two transitions. In contrast, in $CuCrO_2$ the ferroelectric polarization and long-range antiferromagnetic order emerge concomitantly. Thus, it presents an opportunity to study the direct coupling between the magnetic and ferroelectric order parameters [3, 4]. A number of studies have investigated the crystal structure, magnetic excitations, magnetization, and electric polarization in $CuCrO_2$ [3–20], but little is known about the phonons and their coupling or response to the magnetic/ferroelectric ordering.

$CuCrO_2$ is a geometrically frustrated triangular lattice antiferromagnet ($T_N \simeq 24$ K [11]) with delafossite structure (Fig. 1). Although the polarization is thought to arise from proper-screw type magnetic order [21], there is evidence of in-plane structural symmetry breaking across the magnetic transition in several delafossite compounds [7, 22]. This structural distortion arises from magnetoelastic coupling, which is observed in a wide range of hexagonal manganites and delafossites [2, 7, 22–24]. The structural distortion across T_N could possibly change the bonding environment and thus the exchange constants as well as interatomic force constants, thus altering both the spin and phonon dynamics. For instance, in $HoMnO_3$, the shift in position of Mn ions couples with exchange coupling constants, causing a change of cur-

* bansald@ornl.gov
† olivier.delaire@duke.edu

vature of spin waves below T_{SR}, the spin reorientation temperature [23]. Also, recent lattice dynamics studies in $LiCrO_2$ and $CuCrO_2$ report mixed magnon-phonon modes below T_N [25, 26]. Tóth *et al.* [25] observed the appearance of electromagnons below 10 meV with inelastic x-ray scattering in $LiCrO_2$. Park *et al.* [26] focused on spin-waves in $CuCrO_2$ and attributed an intensity change across T_N for a 12.5 meV excitation to a mixed magnon-phonon character. Furthermore, ultrasonic measurements in delafossite compounds have indicated substantial softening of elastic constants near T_N [16, 27]. A possible signature of spin-phonon coupling can also be found in reported thermal conductivity measurements of $YMnO_3$ or $CaMnO_3$ [28–30], motivating studies of the role of the spin-phonon interaction on phonon scattering rates. The strong dynamic coupling between spin fluctuations and phonons in $YMnO_3$ and $CaMnO_3$ lead to suppression of thermal transport in paramagnetic state. Interestingly, the thermal conductivity of polycrystalline $CuCrO_2$ (~5.5 W/mK) is also substantially lower than in the non-magnetic analogue $CuAlO_2$ (~55 W/mK), approximately by a factor of ten at room temperature. Accurate phonon measurements and simulations constitute the basis to understand the thermal transport behavior.

We have investigated the spin and lattice dynamics of $CuCrO_2$ using neutron and x-ray scattering, complemented with first-principles lattice dynamics simulations. We show that lattice distortions across T_N do not discontinuously alter the lattice dynamics, as is expected considering the very small magnitude of the distortion ($\Delta L/L \sim -3\times10^{-4}$ [7]). Raman measurements also found no discontinuity across T_N [16]. However, we find that low-energy spin fluctuations do lead to increased phonon scattering rates above T_N. We quantify the phonon scattering rates from several phonon scattering mechanisms to understand the low value of lattice thermal conductivity (κ_L) of $CuCrO_2$ in comparison to the non-magnetic delafossite $CuAlO_2$. Moreover, our measurements and simulations of phonon spectra show that Cu vibrations exhibit strong anisotropy between in- and out-of-plane directions, which is confirmed by our neutron diffraction measurements of the atomic displacement parameters. In addition, we observed a systematic temperature dependence of phonon intensities (normalized for Bose-Einstein factor) for low-energy modes, but this behavior appears decoupled from the magnetic ordering.

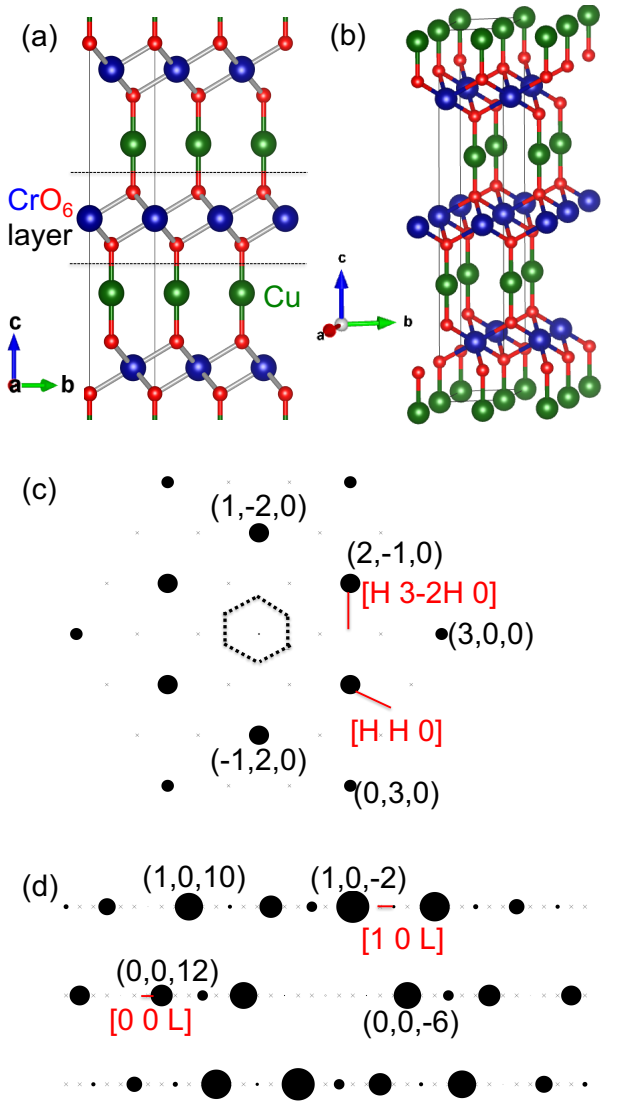

FIG. 1. (a,b) CrO_6 octahedra layers linked through O-Cu-O dumbbells forming the hexagonal crystal structure ($R\bar{3}m$, space group: 166) of $CuCrO_2$. The Cr, Cu, and O atoms are represented by blue, green, and red color, respectively. c) HK0, and d) H0L scattering plane of $CuCrO_2$. The size of black circles correspond to x-ray scattering intensity. Black dotted lines in subfigure (b) denote the Brillouin zone. The red lines show subset of high symmetry directions along which phonon dispersion are plotted in Fig. 6.

II. EXPERIMENTS

A. Sample Preparation and Thermal Conductivity Measurements

Powder and small single-crystal samples were grown by a flux method as described in Ref. 6. The single-crystal samples are of high quality, with mosaic less than 0.05 degree as shown by the representative x-ray rocking curve in Fig. 2-a. The in-plane thermal conductivity was measured in a Quantum Design Physical Property Measurement System; four gold-coated copper leads were attached to the sample via silver epoxy.

B. Inelastic Neutron Scattering

Inelastic neutron scattering (INS) measurements on $CuCrO_2$ powders were carried out using the time-of-flight wide angular-range chopper spectrometer (ARCS) and the cold neutron chopper spectrometer (CNCS) at the Spallation Neutron Source (SNS) at Oak Ridge National Laboratory [31]. The powder (mass ~ 8 g) was encased in a thin-walled aluminum can. We used a closed-cycle helium refrigerator and a low-background resistive furnace with an oscillating radial collimator for low temperature ($10 \le T \le 300$ K) and high temperature ($300 \le T \le 530$ K) measurements, respectively. The empty aluminum can was measured in identical conditions at all temperatures. Four incident neutron energies, E_i=12 and 25 meV at CNCS, and 55 and 120 meV at ARCS were used at each temperature to probe the full phonon and spin wave spectra with high resolution. The energy resolution (full width at half maximum) for incident energies E_i = 12, 25, 55, and 120 meV is ~0.6, 1.2, 2.2, and 6.1 meV at the elastic line, respectively, which reduces to 1.2 and 5.1 meV at an energy transfer of 30 meV for E_i = 55, and 120 meV.

The measured signal was transformed from instrument coordinates, scattering angle and neutron detection times, to the physical momentum transfer, $|\boldsymbol{Q}|$, and energy transfer, E, using the MANTID software [32]. Subsequently, two-dimensional intensity maps for the dynamical susceptibility $\chi''(\mathbf{Q}, E)$ were calculated from the dynamical structure factor $S(\mathbf{Q}, E)$ using $\chi''(\mathbf{Q}, E) = (1 - \exp(-E/k_{\rm B}T))S(\mathbf{Q}, E)$. The phonon density of states (DOS) was obtained from 120 meV data by integrating over $5 \leqslant |\boldsymbol{Q}| \leqslant 10$ Å^{-1}, and applying background and multi-phonon scattering corrections and removing the elastic peak as described in Ref. 33.

The phonon spectra from INS measurements are weighted by the relative neutron scattering strengths (σ/m) of the elements present in the sample, where σ is the neutron scattering cross-section, and m the atomic mass. The neutron weighting (NW) factors for Cr, Cu, and O are σ_{Cr}/m_{Cr} = 0.0671, σ_{Cu}/m_{Cu} = 0.1264, and σ_O/m_O = 0.2645, respectively (in units of barns/amu). Consequently, the total phonon DOS measured with INS, $g(E)$, for $CuCrO_2$ is over-weighted for the Cu and O vibrational contributions:

$$g_{NW}(E) = \left(\frac{\sigma_{Cr}}{m_{Cr}} g_{Cr}(E) + \frac{\sigma_{Cu}}{m_{Cu}} g_{Cu}(E) + 2\frac{\sigma_O}{m_O} g_O(E)\right) / \left(\frac{\sigma_{Cr}}{m_{Cr}} + \frac{\sigma_{Cu}}{m_{Cu}} + 2\frac{\sigma_O}{m_O}\right) \quad (1)$$

where g_{Cr}, g_{Cu}, and g_O are the partial DOS of Cr, Cu, and O, respectively. The resulting NW phonon DOS can be directly compared against the simulated DOS to which the same neutron weights are applied. We should mention here that full expression of phonon DOS, $g_{NW}(E) \propto \sum_d g_d(E) \exp(-2W_d) \exp(2W) \frac{\sigma_d}{m_d}$, includes atom specific $(\exp(-2W_d))$ and average $(\exp(-2W))$ Debye-Waller factor correction. We have approximated $\exp(-2W_d + 2W)$ as unity.

C. Inelastic X-ray Scattering

We used high-resolution inelastic x-ray scattering (IXS) to measure phonon dispersion curves of $CuCrO_2$ on a small single crystal of approximately ~ 100 μm thickness. The experiments were conducted at beamline 30-ID-C (HERIX [34, 35]) at the Advanced Photon Source (APS). The highly monochromatic x-ray beam of incident energy $E_i \simeq 23.7$ keV (λ = 0.5226 Å) had an energy resolution $\Delta E_i \sim 1.0$ meV (full width at half maximum), and was focused on the sample with a beam cross-section ~ 35 × 15 μm (horizontal×vertical). The convoluted energy resolution of the monochromatic x-ray beam and analyzer crystals was $\Delta E \sim 1.5$ meV. The crystal was glued to a copper post using varnish, and mounted in a closed-cycle helium refrigerator. The measurements were performed in the transmission geometry. Typical counting times were in the range of 40 to 120 s at each point in the energy scans at constant $\boldsymbol{Q}$.

The orientation matrix was defined using (1,1,0) and (0,0,$\bar{6}$) Bragg peaks, and checked with other peaks. The longitudinal and transverse acoustic dispersions were measured along high symmetry directions $(\xi, 0, \bar{6})$, $(\xi, \xi, \bar{6})$, (1+ξ, 1+ξ, 0), $(2, \bar{1}, -6+\xi)$, $(1, 0, -5+\xi)$, $(1, 1, -6+\xi)$, $(0, 0, 12+\xi)$, $(\xi, 3-2\xi, 0)$, and $(\xi, 1, \xi-1)$. The spectra were fitted with a damped-harmonic-oscillator (DHO) scattering function [36], subsequently convoluted with the measured instrumental resolution function, $R * S(E)$:

$$S(E) = A \frac{\{\frac{1}{2} \pm \frac{1}{2} + n(|E|)\} \times \frac{1}{2}\Gamma_{LW} E}{(E^2 - E_0^2)^2 + (\frac{1}{2}\Gamma_{LW} E)^2} + B\,, \quad (2)$$

where B is a constant background, $n(E)$ is the temperature-dependent Bose-Einstein distribution at energy transfer E, A is the amplitude, Γ_{LW} is the full width at half maximum of the phonon peak, and E_0 is the bare phonon energy in the absence of damping (the + sign is for $E > 0$ and the − sign for $E < 0$). Example IXS spectra and the corresponding DHO fits are shown in Fig. 2-(b,c).

D. Neutron Diffraction

Neutron time-of-flight powder diffraction measurements were carried out using the POWGEN diffractometer at the Spallation Neutron Source [37] using the same powder sample described in Sec. II B, with the sample encased in a thin-walled vanadium can. A top loading closed cycle refrigerator with a heating stick was used for temperature control. Data were collected with the center wavelength 0.533 and 2.665 Å, allowing access to a d-spacing range from 0.5 to 10 Å. Data were collected at 40, 80, 150, 200, 300, 420 K.

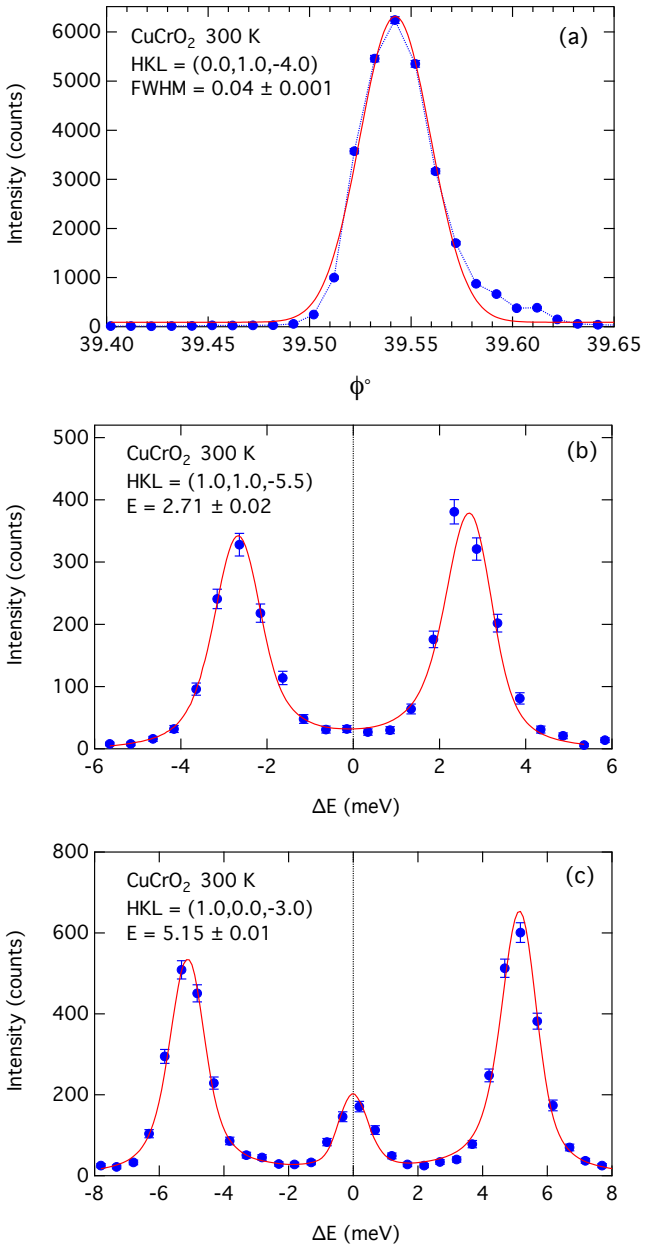

FIG. 2. (a) Rocking curve of $CuCrO_2$ single crystal for bragg peak at $\boldsymbol{Q}$ = (0.0, 1.0, −4.0) showing the high quality of the crystal. (b) Constant-$\boldsymbol{Q}$ inelastic x-ray scattering spectra for in-plane polarized transverse acoustic mode at $\boldsymbol{Q}$ = (1.0, 1.0, −5.5) at 300 K. The lines are fits using a damped harmonic oscillator profile convoluted with the instrument resolution (see text). The value of E (in meV) listed in inset is the fitted phonon energy. Negative ΔE corresponds to phonon annihilation, and positive ΔE to phonon creation. (c) Same as (b) for $\boldsymbol{Q}$ = (1.0, 0.0, −3.0).

The data were reduced using standard algorithms in the MANTID package [32]. Data were refined using the GSAS and EXPGUI packages [38, 39] using the model described in Ref. 10 as a starting model. Standard profile parameters employing the GSAS profile type 3 [38, 40] were refined at low temperature and held fixed for the remainder of the temperature refinements. We did not consider magnetic scattering in the refinement process as magnetic intensity is minimal at large $|\mathbf{Q}|$ and the measurements were conducted above T_N. For all refinements, the goodness of fit value (R_{wp}) were less than 0.055. Lattice parameters and anisotropic atomic displacement parameters were refined at all temperatures. The lattice parameters exhibit temperature behaviors consistent with literature values, with the c-axis displaying a negative thermal expansion, and the a-axis displaying normal thermal expansion [10, 41].

III. DENSITY FUNCTIONAL THEORY SIMULATIONS

First-principles simulations were performed in the framework of density functional theory (DFT) as implemented in the Vienna *Ab initio* Simulation Package (VASP 5.3) [42–44]. A $12\times12\times12$ Monkhorst-Pack electronic k-point mesh with a plane-wave cut-off energy of 500 eV was used in all of our simulations. The projector-augmented-wave potentials explicitly included six valence electrons for Cr ($3d^5 4s^1$), 11 for Cu ($3d^{10}4s^1$), and six for O ($2s^2 2p^4$). All our calculations were spin polarized (collinear). We used the generalized gradient approximation (GGA) in the Perdew-Burke-Ernzerhof (PBE) parametrization [45] with a Hubbard correction. To treat the localized d−electron states of Cr in GGA+U calculations, the total energy expression was described as introduced by Dudarev *et al.* [46] with on-site Coulomb interaction U = 2.3 eV and on-site exchange interaction J = 0.96 eV [15, 47, 48].

During the relaxation of the structure, the lattice parameters and atomic positions were optimized until forces on all atoms were smaller than 1 meV Å^{-1}. The relaxed lattice parameters (a = 3.026 Å, c = 17.166 Å) differed from the experimental values measured at 10 K [10] less than 0.5% along c axis and 2% in-plane. The relaxation of lattice parameters without spin-polarization leads to significant in-plane contraction (a = 2.738 Å) and out-of-plane expansion (c = 18.396 Å) with zero band-gap. Calculations of phonon dispersions were performed in the harmonic approximation, using the finite displacement approach as implemented in Phonopy [49], using the atomic forces obtained with VASP. The phonon calculations used a $3\times3\times3$ supercell of the rhombohedral primitive cell containing 108 atoms, and a $3\times3\times1$ supercell of the hexagonal conventional cell also containing 108 atoms. To construct the force-constant matrix using the finite displacement approach, four independent atomic displacements were computed for both rhombo-

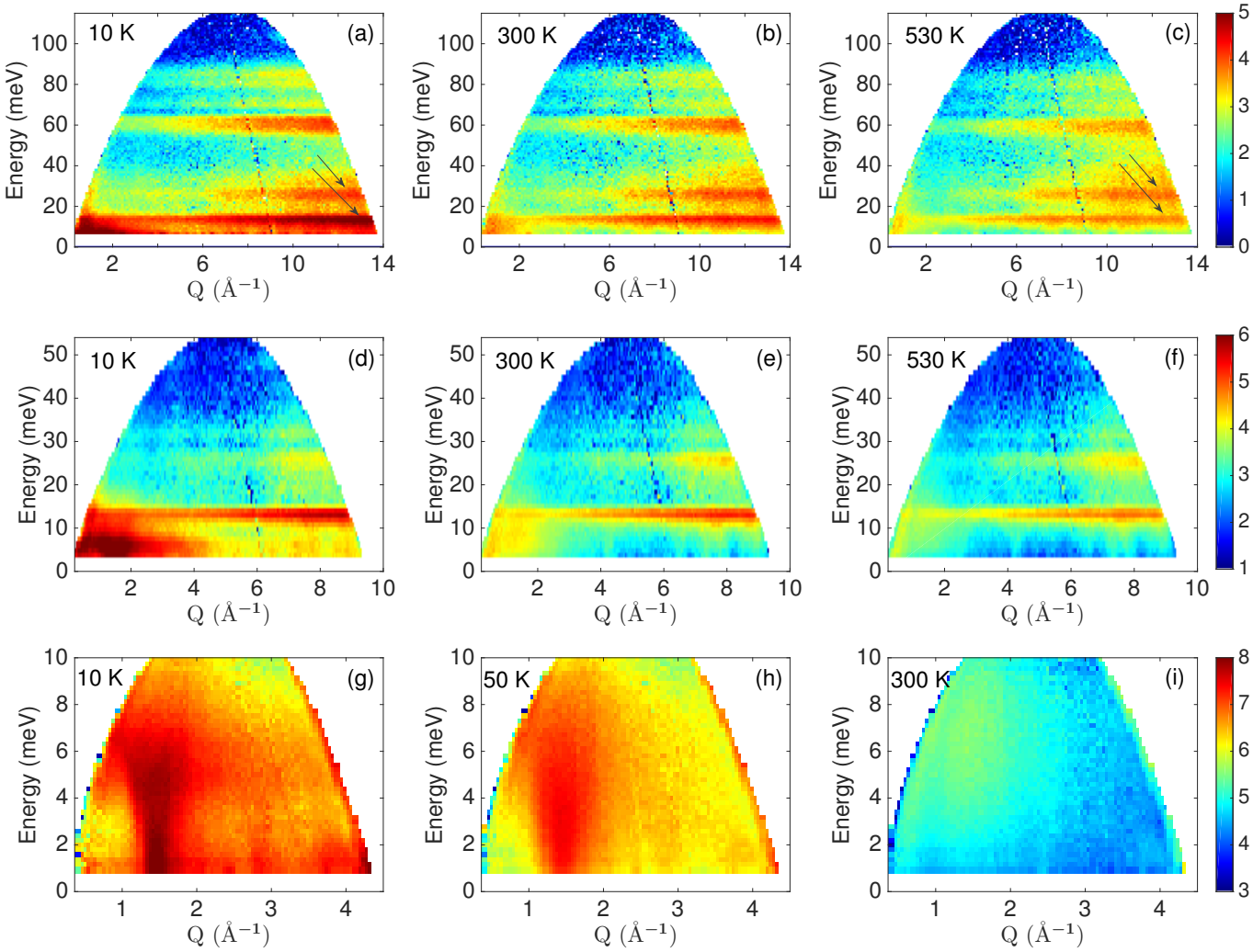

FIG. 3. (a,b,c) The neutron scattering intensity $\chi''(\mathbf{Q}, E) = (1 - \exp(-E/k_{\mathrm{B}}T))S(\mathbf{Q}, E)$ (in log scale) of $CuCrO_2$ measured at different temperatures for an incident energy of 120 meV. (d,e,f) and (g,h,i) are same as (a,b,c) except for an incident energy of 55 and 12 meV, respectively. Subfigures (a-f) are measured on ARCS, while subfigures (g-i) are measured on CNCS. The intense elastic scattering intensity around zero energy transfer is cropped.

hedral and hexagonal cell. The atomic displacement amplitude was $1/100^{th}$ of the lattice parameters.

IV. RESULTS AND DISCUSSION

A. Phonon and Magnon Spectra

Figure 3 shows $\chi''(\mathbf{Q}, E)$ from INS for multiple E_i settings and temperatures. The intensity for $|\boldsymbol{Q}| < 5$ Å^{-1} and $E < 15$ meV is dominated by spin excitations. On the other hand, phonon excitations are intense at high $|\boldsymbol{Q}|$. The maximum phonon energy is around 90 meV. The NW phonon DOS from E_i=120 meV dataset is shown in Fig. 4, where it is compared with the NW phonon DOS from our DFT simulations. The agreement between the experimental data and the DFT simulations is remarkable (the NW DOS is shown as continuous trace at the bottom of figure 4). Phonon dispersions from IXS confirm this good agreement of phonon energies, as shown below. However, two unusual features can be observed in the INS data. First, the magnetic intensity from spin fluctuations persists up to 300 K, far above $T_N \simeq 24$ K (see Fig. 3-(h,i)). Second, the intensity of the phonon peak at ~13 meV in the phonon DOS decreases on heating, while the intensity of the peak at ~25 meV increases.

We first investigate the temperature dependence of the phonon DOS. We note that, while the elastic constants, in particular C_{66}, are reported to soften by approximately 30% near T_N [16], we do not observe any abrupt change in the phonon DOS between 10 and 40 K in our INS measurements (see Fig. 4). This could be because ultrasound

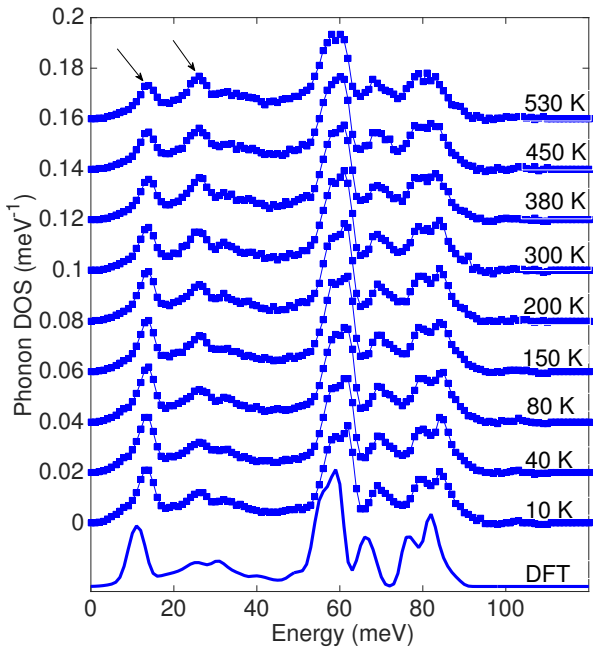

FIG. 4. Neutron-weighted phonon DOS of $CuCrO_2$ measured with inelastic neutron scattering at different temperatures (corrected for background, and multiphonon and multiple scattering) for incident neutron energies of 120 meV ($5 \leq |Q| \leq 10\,\text{Å}^{-1}$) along with DFT calculated neutron weighted phonon DOS convoluted with ARCS resolution function which highlights the good agreement between experiment and simulations.

measurements probe a much lower frequency and longer wavelength range than accessible in these INS measurements. Our results indicate that the overall chemical bonding environment remains largely unaltered across T_N, at least at short distances. The phonon dispersions from IXS also do not show any unusual change for the short wavelength phonons across T_N (see below and Fig. 6). However, as can be seen in Fig. 4, the peaks at ~13 and 25 meV in the DOS show an unusual exchange of intensity with increasing temperature, with the relative ratio of intensity reversed between 10 and 530 K. This can also be seen in $\chi''(\mathbf{Q}, E)$ data (see arrows in Fig. 3-a and c). We note that this apparent exchange of intensity between the two peaks does not change abruptly across T_N but rather occurs gradually, and is thus likely not associated with the magnetic transition. Instead, this behavior is likely due to the strongly anisotropic structure, with the Debye-Waller (DW) factor suppressing the intensity of Cu motions with larger in-plane amplitude at low frequency, as shown below. We note that our reduction procedure to extract the DOS from $\chi''(\mathbf{Q}, E)$ assumes an isotropic and atom-independent DW factor, and thus anisotropic DW effects in χ'' are carried over instead of being corrected for.

The comparison between measurements and simulations enables us to assign various phonon peaks observed in the DOS to contributions from specific atoms and eigenvectors. Figure 5-(a,b,c) shows the partial, and in- and out-of-plane projected phonon DOS for each species. The low-energy phonon peaks are primarily occupied by Cu and Cr vibrations, while the high energy peaks represent oxygen modes. In particular, it is interesting to observe that Cu vibrations are strongly anisotropic, with a large in-plane Cu amplitude dominating the 13 meV peak in the DOS, while the peak at 25 meV is mostly arising from Cu out-of-plane vibrations, with some Cr component as well. The in-plane Cu vibrations have a large amplitude, as we show in our measurements and analysis of atomic displacement parameters below. This anisotropy of vibration amplitudes affects the measured inelastic intensities via the DW factor. The expression for $\chi''(\mathbf{Q}, E)$ for single phonon creation is given by [50]:

$$\chi''(\mathbf{Q},E) \propto (1-\exp(-\frac{E}{k_B T})) \sum_s \sum_\tau \frac{1}{\omega_s} \left| \sum_d \frac{\overline{b_d}}{\sqrt{M_d}} \exp(-W_d) \exp(i\mathbf{Q}\cdot\mathbf{d})(\mathbf{Q}\cdot\mathbf{e}_{ds}) \right|^2 \times \langle n_s+1 \rangle \delta(\omega-\omega_s)\delta(\mathbf{Q}-\mathbf{q}-\tau) \quad (3)$$

where $\overline{b_d}$ is neutron scattering length, $\boldsymbol{Q} = \boldsymbol{k} - \boldsymbol{k}'$ is the wave vector transfer, and $\boldsymbol{k}'$ and $\boldsymbol{k}$ are the final and incident wave vector of the scattered particle, $\mathbf{q}$ the phonon wave vector, ω_s the eigenvalue of the phonon corresponding to the branch index s, τ is the reciprocal lattice vector, d the atom index in the unit cell, $\exp(-2W_d)$ the corresponding DW factor, and n_s the mean Bose-Einstein occupation factor. The atom-resolved DW factor clearly reflects the underlying anisotropy of vibrational modes through the phonon polarization vectors $\mathbf{e}_{ds}$ and their associated frequencies ω_s [50]:

$$W_d(\mathbf{Q}) = \frac{\hbar}{4M_d N} \sum_s \frac{|\mathbf{Q}\cdot\mathbf{e}_{ds}|^2}{\omega_s} \langle 2n_s+1 \rangle \quad , \quad (4)$$

with M_d the atomic mass and N the number of atoms. As one can see, for large in-plane Cu vibrations, $|\mathbf{Q}\cdot\mathbf{e}_{ds}|^2$ will be significantly larger than for out-of-plane vibrations, thus leading to their larger suppression in $\chi''(\mathbf{Q}, E)$ through $\exp(-2W_d)$.

We now focus on phonon dispersions and intensities obtained from IXS measurements. Figure 6 shows the

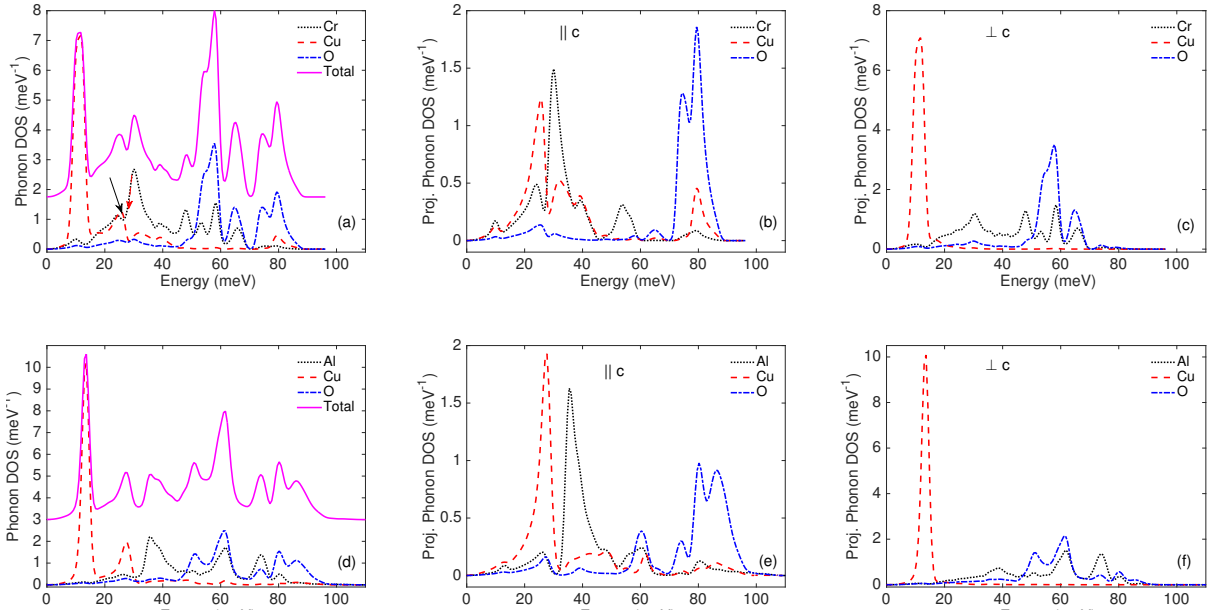

FIG. 5. a) Partial and total phonon DOS, b) out-of-plane, and c) in-plane projected partial phonon DOS of $CuCrO_2$ calculated from DFT simulations. Subfigure (d,e,f) same description as (a,b,c) for $CuAlO_2$.

phonon dispersions of $CuCrO_2$ along high symmetry directions, measured with IXS at multiple temperatures, and computed with DFT. The agreement between experiment and theory is quite good, especially for phonons propagating along the c-axis. From Fig. 6, we do not observe any discernible change in measured phonon energies between 7 and 300 K (within the experimental resolution). Although the phonon energies do not shift significantly, phonon intensities show a departure from the T dependence of intensities expected from the Bose-Einstein occupation factor in the harmonic phonon picture. As shown in Fig. 7-(a,c,e), the phonon intensity of in-plane propagating phonons (LA along [HH0], and TA along [H0$\bar{6}$] and [HH$\bar{6}$]) at 300 K is lower than at 7 K by nearly 30%. On the contrary, the intensity of out-of-plane propagating phonons (LA along [00L], and TA along [10L] and [11L]) increases by approximately 10-40% from 7 to 300 K (Fig. 7-(b,d,f)). An analogous behavior is seen in $\chi''(\mathbf{Q}, E)$ from INS (Fig. 3-(a,b,c)). A more detailed analysis of $\chi''(E)$ intensity from INS data (corrected for background, not corrected for multiphonon scattering) is presented in Fig. 8-(a,b) for multiple incident energies. The observed suppression in intensity of the ~13 meV phonon peak from 10 to 300 K is approximately 35% (Fig. 8-c), consistent with IXS measurements. We note that the T-dependence of the phonon intensity of ~13 meV peak in our DOS measurements differs from the observation by Park *et al.* [26], who reported no change in the phonon intensity at ~13 meV above T_N along [H,H,0] for $\frac{1}{3} \leqslant \mathrm{H} \leqslant \frac{2}{3}$.

Figure 3-(d-i) shows $\chi''(\mathbf{Q}, E)$ at low $|\mathbf{Q}|$ zooming on magnetic excitations (12 meV data). As one can observe, the magnetic intensity extends from 0 to 15 meV for $|\mathbf{Q}| < 5\text{Å}^{-1}$, and remains visible up to 300 K, far above $T_N \simeq 24$ K. Even the 55 meV data measured at 530 K show some remnant magnetic intensity at low $|\mathbf{Q}|$, see Figure 3-f. A similar observation was also reported by Poienar *et al.* [9], but their measurements were limited to low temperatures ($\mathrm{T} \leqslant 40$ K). We show the temperature dependence of magnetic intensity between $2.25 \leqslant E \leqslant 11$ meV in Fig 8-d. The magnetic intensity decreases to 55% at 80 K compared to the value at 10 K, and suprresses to 10% at 400 K indicating the weakening of time-correlations between spin-fluctuations with increasing T.

The T-dependence of phonon intensities in $\chi''(\mathbf{Q}, E)$ can be compared to the vibrational anisotropy information encoded in the mean square thermal displacements. The thermal displacement, $\langle |U_d^\alpha|^2 \rangle$, can be calculated from the DFT phonon simulations, in the harmonic approximation:

$$\langle |U_d^\alpha|^2 \rangle = \frac{\hbar}{2NM_d} \sum_s \omega_s^{-1} \langle 1 + 2n_s \rangle |\mathbf{e}_{ds}^\alpha|^2 \qquad (5)$$

where α denotes thermal displacement direction. The temperature dependence of $\langle |U_d^\alpha|^2 \rangle$ for Cu is shown in Fig. 9. The DFT values are also compared with $\langle |U_d^\alpha|^2 \rangle$ extracted from our neutron diffraction experiments, and results from Poienar *et al.* [10]. As one can see, the general agreement between DFT and experiment is rather good. The slope of the T dependence is well captured. Offsets can arise from the experimental Rietveld refinement procedure (possibly from texture in the powders) or from static displacements in the sample associated with

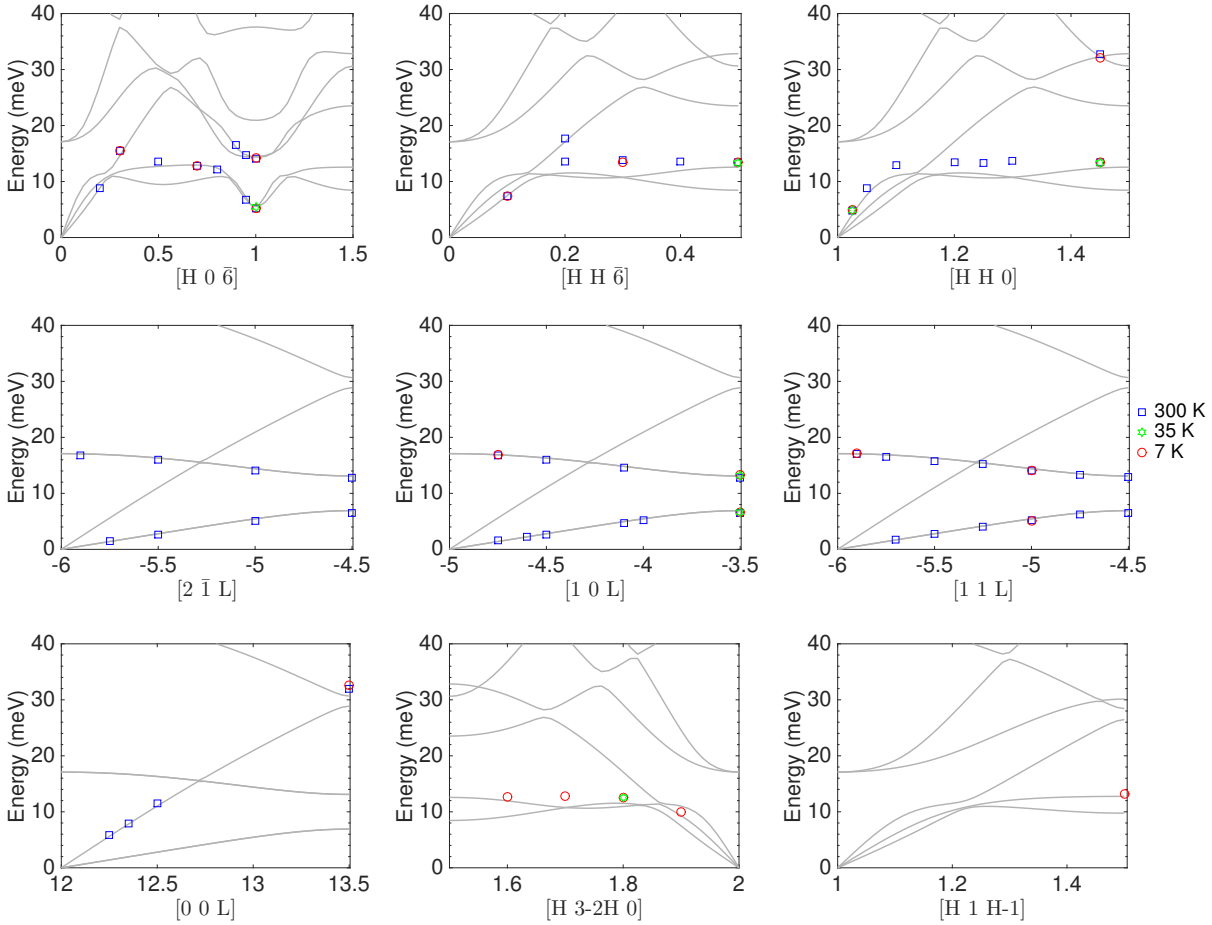

FIG. 6. Phonon energies of $CuCrO_2$ obtained from experimental inelastic x-ray scattering measurements at three different temperature points (■: 300 K, ★: 35 K, and •: 7 K). The light-gray lines are DFT simulations of phonon dispersions for $CuCrO_2$ along high symmetry directions. Error bar in experimental measurements is smaller than the size of the symbols used. A subset of measurement directions are shown in Fig. 1-(b,c).

strains or impurities. The strong anisotropy of Cu in-plane vibrations (Fig. 5-(d,e,f)) at low T is a characteristic feature of delafossite compounds as corroborated by measurements on $CuAlO_2$ and $CuFeO_2$ [51, 52]. Within the accuracy of the data, we note a possible change in the anisotropy ellipse for Cu vibrations with increasing T in $CuCrO_2$, which could reflect the anisotropic expansion/contraction of lattice parameters. Previous studies (Ref. 10) and our own neutron diffraction measurements show that $CuCrO_2$ exhibits a contraction in c lattice parameter between 0 K and 300 K, which is considerably larger (two to ten times larger) than in other non-magnetic delafossite compounds (AMO_2 – A = Cu, Ag; M = Al, Sc, In, or La)[51]. In addition, by comparing $\langle|U_d^\alpha|^2\rangle$ for $CuAlO_2$ (Fig. 9-b), one can see that Cu vibrations in $CuAlO_2$ are well captured by the harmonic DFT simulations and remain strongly anisotropic with increasing T, while in $CuCrO_2$ the U_{11} value becomes closer to U_{33} than predicted by DFT.

B. Thermal Conductivity

The thermal conductivity (κ) of $CuCrO_2$ is known to be low (~5.5 W/mK at T = 300 K) and exhibits an unusual T-dependence, as previously observed in powder measurements [14], and confirmed for in-plane κ in our single-crystal measurement (see below). For comparison, the reported κ measured on a powder sample of the similar delafossite $CuAlO_2$ exceeds 50 W/mK at room temperature [53] despite the phonon group velocities (v_g) in $CuCrO_2$ and $CuAlO_2$ of similar magnitude (see Table I). Our in-plane κ measurements in a small $CuCrO_2$ crystal are compared with the previous polycrystalline data [14], and modeled based on our DFT phonon simulations in Fig. 10-b. The surprisingly low value of κ in $CuCrO_2$ prompted us to investigate the phonon scattering mechanisms.

In the absence of electron-phonon and spin-phonon coupling, phonons can be scattered by point-defects,

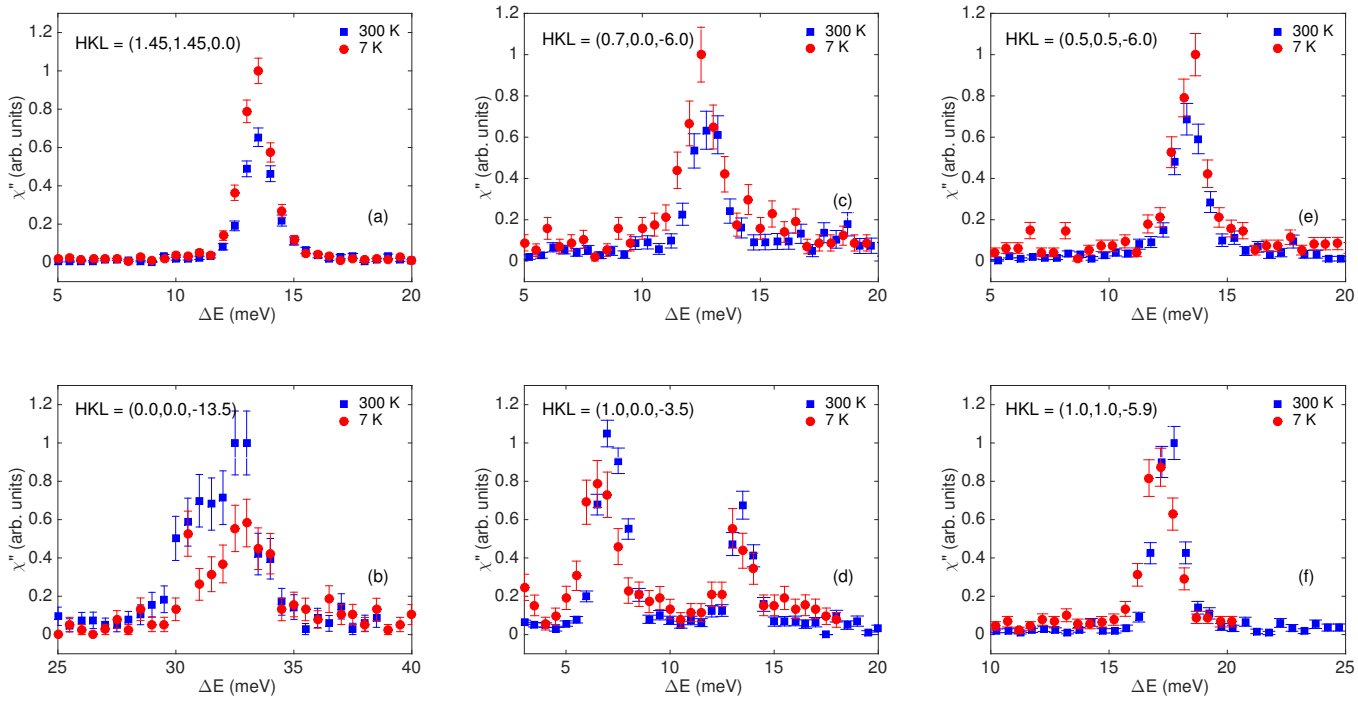

FIG. 7. Constant-$\boldsymbol{Q}$ inelastic x-ray scattering spectra, corrected for thermal occupation factor, for in-plane (a,c,e) propagating phonon mode at $\boldsymbol{Q}$ = (1.45, 1.45, 0.0), (0.7,0.0,-6.0) and (0.5,0.5,-6.0), and out-of-plane (b,d,f) propagating phonon mode at $\boldsymbol{Q}$ = (0.0, 0.0, −13.5), (1.0,0.0,-3.5) and (1.0,1.0,-5.9) with different polarization vector for $CuCrO_2$ at 300 and 7 K. The intensities, $\chi''(\mathbf{Q}, E) = (1 - \exp(-E/k_B T))S(\mathbf{Q}, E)$, are normalized with respect to the incident flux.

TABLE I. Phonon group velocities (v_g in m/s) of long-wavelength acoustic phonons for $CuCrO_2$ and $CuAlO_2$, calculated from DFT simulations.

Direction	Mode	$CuCrO_2$ v_g (m/s)	$CuAlO_2$ v_g (m/s)
[100]	TA1	3392	4211
	TA2	2272	2131
	LA	5333	6412
[110]	TA1	3427	4183
	TA2	2249	1870
	LA	5349	6385
[001]	TA	2154	2992
	LA	9307	10827

boundaries, and other phonons (anharmonicity). If all the scattering processes are independent of each other, then following Matthiessen's rule, the total phonon scattering rate τ^{-1} is the sum of individual scattering rates,

$$\tau^{-1} = \tau_{PD}^{-1} + \tau_B^{-1} + \tau_U^{-1}. \quad (6)$$

where, τ_{PD}^{-1}, τ_B^{-1}, and τ_U^{-1} denote the point-defects, boundary, and phonon-phonon or Umklapp scattering processes. The scattering rates from these scattering mechanisms can be modeled as [54, 55],

$$\tau^{-1} = V\frac{\omega^4}{4\pi v_g^3}\left(\frac{\Delta M}{M}\right)^2 + \frac{v_g}{L} + P\frac{\hbar\gamma^2}{M v_g^2 \theta_D}\omega^2 T^n \exp\left(-\frac{\theta_D}{mT}\right). \quad (7)$$

Here, V is the volume per unit cell, v_g and ω are the phonon group velocity and phonon frequency, $\Delta M/M$ is the point-defect ratio, L is the grain size, θ_D is the Debye temperature, γ is an average Grüneisen parameter, and P, n, and m are Umklapp scattering parameters of order one. For the point-defect scattering, we have not considered the perturbation in force-constants and nearest-neighbor distances. A Debye temperature $\theta_D = 850 \pm 50$ K was estimated by Okuda *et al.* from heat capacity measurements [13]. We have calculated the Debye temperature from the first moment of the measured phonon DOS, as $\theta_D = \frac{4\langle E\rangle}{3k_B}$, where $\langle E\rangle = \int g(E)E\,dE$ and k_B is Boltzmann's constant. We find $\theta_D = 814 \pm 10$ K, and use this value in our κ analysis. The parameters for Umklapp scattering, P, n, and m are kept constant at 1.0, 1.0, and $\sim 2N^{1/3} = 4.54$, respectively. To estimate the boundary scattering, we use the shortest dimension (0.87 mm) of the single-crystal specimen used in our κ measurment. $\gamma = \alpha V K_T/C_v$ is estimated to be 2.26 at T = 300 K, where

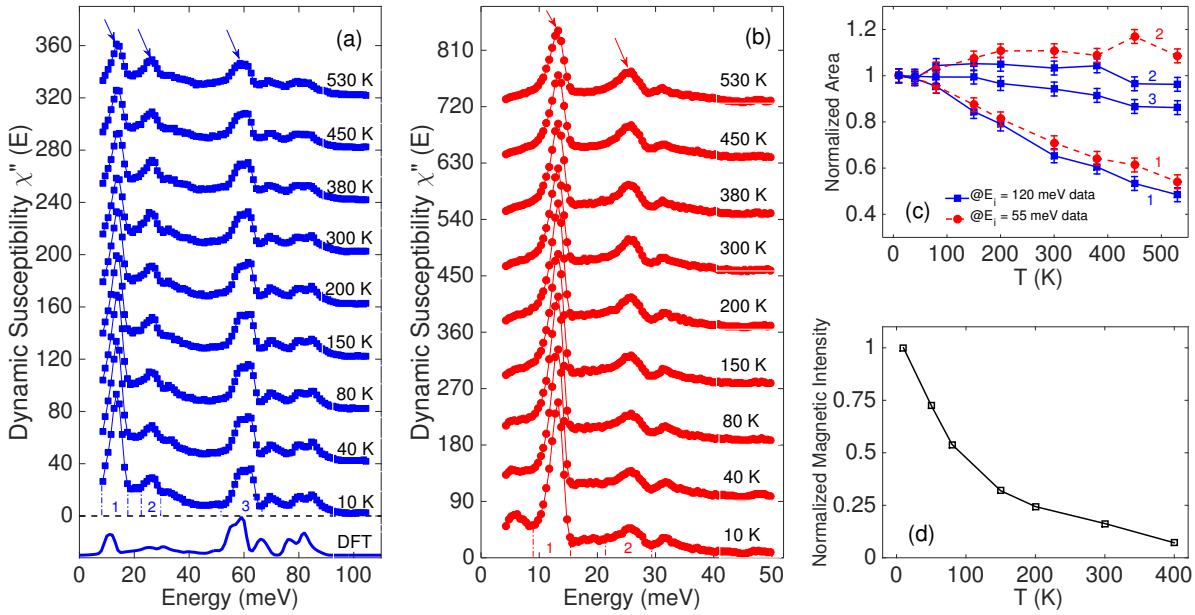

FIG. 8. The neutron scattering intensity $\chi''(E) = (1-\exp(-E/k_BT))S(\mathbf{Q},E)$ of $CuCrO_2$ measured at different temperatures for incident energies of a) 120, and b) 55meV. The results are compared with NW phonon DOS calculated using DFT simulations in subfigure (a) highlighting the good agreement between theory and experiment. The integration range for 120 and 55 meV incident energies are $5 \leqslant |\mathbf{Q}| \leqslant 10$ Å^{-1} and $5 \leqslant |\mathbf{Q}| \leqslant 8$ Å^{-1}, respectively. The small hump in 10 K dataset in subfigure (b) is due to magnetic scattering. Subfigure (c) show the ratio of area under the peak at ~13, ~25, and ~60 meV for $E_i = 120$ and 55 meV. The energy integration ranges for 'Area' are marked in subfigure (a) and (b). Subfigure (d) shows normalized magnetic scattering intensity calculated by integrating the $\chi''(\mathbf{Q},E)$ for $0 \leqslant |\mathbf{Q}| \leqslant 3$ Å^{-1} and $2.25 \leqslant E \leqslant 11$ meV from the $S(\mathbf{Q},E)$ dataset with an incident energy of 25 meV

α is coefficient of volume thermal expansion, V is the unit cell volume, K_T the iso-thermal bulk modulus, and C_v the heat capacity at constant volume (per unit cell). It should be noted that for calculation of γ we consider average value of α, and do not make distinction between in-plane and out-of-plane thermal expansion coefficients. Moreover, the point-defect ratio $\Delta M/M = 0.023$ is found by fitting the low temperature (below 15 K) in-plane κ. The points defects could be due to oxygen vacancies or impurities present in the sample. Given the excellent agreement between the calculated and measured phonon DOS and dispersions, we determined $\boldsymbol{q}$- and direction dependence of the phonon energy and group velocity from our DFT simulations.

The effects of different scattering mechanisms on the orientation-averaged lattice thermal conductivity (κ_L) are shown in Fig. 10-a. As seen in this figure, with only point-defect or boundary scattering, which are independent of T, κ_L increases steeply at low temperatures owing to the increasing heat capacity, and saturates at high temperature. Conversely, umklapp scattering keeps increasing with T and becomes the dominant source of scattering above 100 K. However, the experimental data show that above $T_N \simeq 24$ K, κ_L increases much slower than is predicted from point-defect, boundary, and Umklapp scattering combined. Another important observation is that the peak in the experimental κ_L curve is around 200 K, while point-defect, boundary, and Umklapp scattering alone would give rise to a peak at 50 K (see brown curve in Fig. 10-a labeled 'Total without spin fluctuation'). Thus, these scattering mechanisms are not sufficient to explain the behavior of the measured κ_L. In fact, this model would lead to $\kappa_L \simeq 41.5$ W/mK at 300 K, similar to the value (~ 55 W/mK) observed in $CuAlO_2$ [53].

As described earlier, spin fluctuations in $CuCrO_2$ persist even above room temperature. These spin fluctuations can create strain fields with spatial extent extending to the length of spin correlations, ξ [28]. We use the following assumptions to estimate the phonon scattering from spin fluctuations. If spin fluctuations have slower time scale than lattice vibrations, they can act as scattering center of spherical object of size ξ with scattering cross-section given by $\pi(\xi/2)^2$ in the limit of $\lambda_p \ll \xi$, where λ_p is the phonon wavelength [28]. The scattering rate from spin fluctuations can be obtained by multiplying scattering cross-section with density of scatterers ρ_0, and phonon group velocity v_g, such that –

$$\tau_{SF}^{-1} = \rho_0 v_g \pi(\xi/2)^2 = C_{SF} v_g, \tag{8}$$

where $C_{SF} = \rho_0 \pi(\xi/2)^2$. Taking C_{SF} as a free parameter, by matching the peak in the experimental thermal

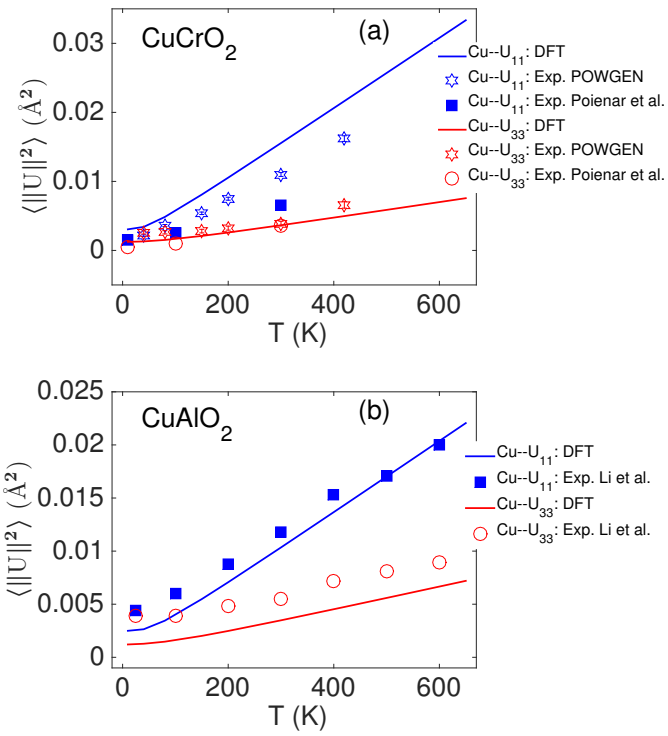

FIG. 9. The increase in mean square thermal displacement of Cu atom in a) $CuCrO_2$, and b) $CuAlO_2$ with temperature calculated from DFT simulations compared against experimental neutron diffraction measurements of Poienar *et al.* [10] and Li *et al.* [51], respectively.

conductivity data, we obtain $C_{SF} = 2.5\times10^7$ (1/m). For ξ = 40 Å, the average distance, $d = 2(3/4\pi\rho_0)^{1/3}$, between two scatterers will be ~ 99 Å, greater than ξ, required for self-consistency. These values are comparable to the values (ξ ~ 20-50 Å) reported in Ref. 28 and 29. Below T_N, in a long-range ordered state, ξ will diverge to infinity, and the scattering rate will approach zero. Hence, in our calculations we have only included scattering from spin fluctuations above T_N. The phonon scattering from spin fluctuations is shown in Fig. 10-a. As seen on this figure, our model reproduces the suppression, slow rise, and large shift in the temperature of the peak in κ_L, indicating a pronounced scattering of phonons by spin fluctuations, similar to previous observations in $YMnO_3$ [28]. We note that we could not extract any reliable values for the linewidths Γ_{LW} from the experimental IXS spectra, which were resolution limited. From our modeling, the expected Γ_{LW} for phonons with large v_g range from 0.01 to 0.3 meV, much smaller than the instrument resolution. Because of approximations in expressions for the phonon scattering rate [54, 55], our model is not expected to correctly predict linewidths away from zone-center, where v_g is small, but these modes contribute very little to κ_L anyway.

Motivated by the anisotropy of atomic vibrations described above, we have also investigated the anisotropy of κ_L, as shown in Fig. 10-b. The longitudinal acoustic (LA) phonons propagating along c have a significantly larger group velocity than LA phonons propagating in-plane (see Table I; and further confirmed by good agreement of the calculated elastic constants C_{11} = 16.0×10^{10} N/m^2 and C_{33} = 48.7×10^{10} N/m^2 obtained from v_g with the reported experimental data in literature, $C_{11} = 24.2\times10^{10}$ N/m^2 and $C_{33} = 47.0\times10^{10}$ N/m^2 [56]), thus the theoretical κ_L is higher along c than in-plane. The higher value of the out-of-plane κ_L in comparison to the in-plane κ_L is also experimentally measured in hexagonal $YMnO_3$ and $HoMnO_3$ due to larger out-of-plane v_g [28, 57]. It should be noted that we have assumed spin-fluctuation scattering to be isotropic. Experimental measurements of the out-of-plane κ_L are challenging owing to the small size of single crystals. Moreover, the discrepancy between our single crystal measurement and powder measurement of Okuda *et al.* [14] could be due to difference in oxygen stoichiometry, grain size, and non-homogeneity. We attempted the modeling of powder measurements, and found increase in point-defect ($\Delta M/M$ = 0.035) and spin-fluctuation parameter ($C_{SF} = 5.5\times10^7$ (1/m)).

V. SUMMARY

In summary, we have investigated the lattice dynamics of multiferroic $CuCrO_2$ with a combination of INS on a polycrystalline sample and IXS on a crystal, and first-principles phonon calculations, as well as thermal transport measurements. Based on our experiments and modeling, we evaluated the effect of spin-phonon coupling on the phonons and lattice thermal conductivity. Our IXS and INS measurements, sampling a large range of wavevectors, show little effect of spin-phonon coupling on the phonon frequencies across T_N, in agreement with prior Raman reports for zone-center phonons [16]. Our INS and neutron diffraction measurements revealed strongly anisotropic Cu vibrations, with larger amplitudes parallel to the basal plane of the delafossite structure than normal to it. The anisotropy ellipse for Cu vibrations is weakly T-dependent. This behavior is compatible with observations in other delafossite compounds. In addition, we observed a systematic temperature dependence of neutron and x-ray scattering intensities for low-energy phonon modes ($\chi''(\mathbf{Q}, E)$ – normalized for Bose-Einstein factor), but this behavior appears decoupled from the magnetic ordering. Instead, we attribute this deviation to the large in-plane vibrations that suppress phonon intensity via the Debye-Waller factor. Furthermore, modeling of the thermal conductivity shows that the spin fluctuations above T_N are a potent source of phonon scattering, leading to a low κ_L, with a slowly rising temperature dependence. This unusual T-dependence of κ_L in $CuCrO_2$ is markedly different from that in the non-magnetic analogue $CuAlO_2$. Be-

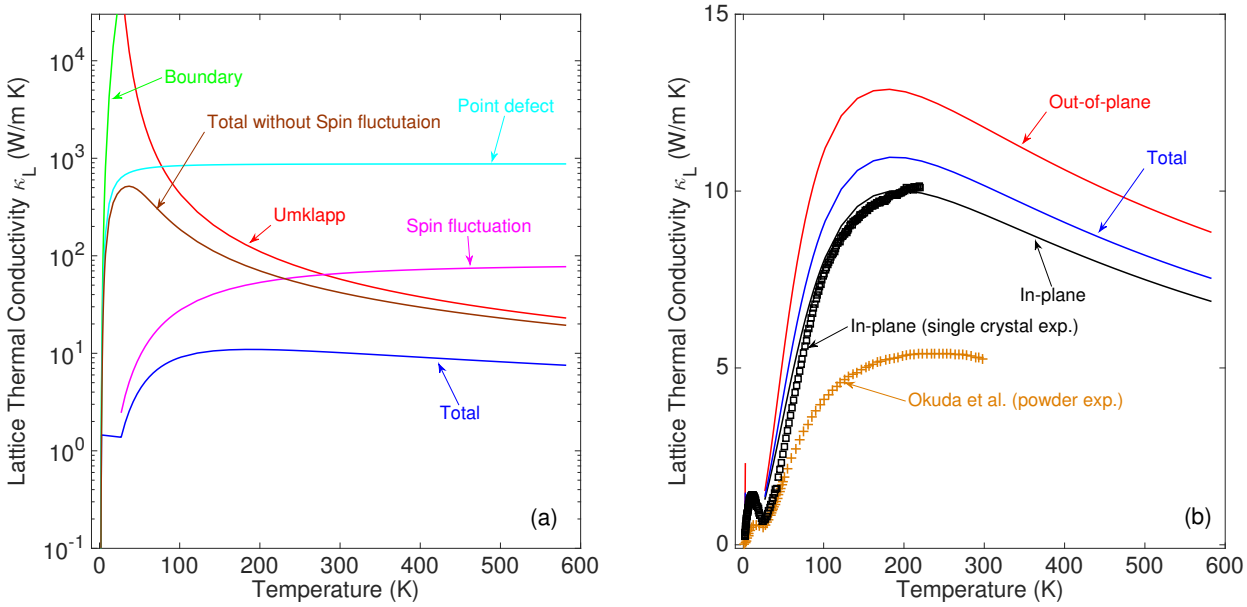

FIG. 10. a) The orientation-averaged lattice thermal conductivity κ_L of $CuCrO_2$ ("Total"), and components considering only certain scattering mechanisms, and b) contribution of in-plane and out-of-plane κ_L to the total κ_L compared with our experimental single crystal measurements and powder data of Okuda *et al.* [14].

sides providing lattice dynamics information for a wide range of temperature, our measurements of phonon dispersions with IXS and INS also clearly distinguish between phonon and magnon intensities, which is crucial in understanding spin-phonon coupling across T_N in this class of spin driven multiferrorics [25, 26].

VI. ACKNOWLEDGEMENTS

We thank John Tischler for help with software to fit the HERIX data. X-ray scattering measurements and first-principles simulations were supported by the U.S. Department of Energy, Office of Science, Basic Energy Sciences, Materials Sciences and Engineering Division, under the Early Career Award No. DE-SC0016166. Neutron scattering measurements were supported as part of the S3TEC EFRC, an Energy Frontier Research Center funded by the U.S. Department of Energy, Office of Science, Basic Energy Sciences under Award No. DE-SC0001299. A.F.M. acknowledges the support from the U.S. Department of Energy, Office of Science, Basic Energy Sciences, Materials Sciences and Engineering Division. H.D.Z thanks the support from NSF-DMR-1350002. The use of Oak Ridge National Laboratory's Spallation Neutron Source was sponsored by the Scientific User Facilities Division, Office of Basic Energy Sciences, U.S. DOE. This research used resources of the Advanced Photon Source, a U.S. Department of Energy (DOE) Office of Science User Facility operated for the DOE Office of Science by Argonne National Laboratory under Contract No. DE-AC02-06CH11357. Theoretical calculations were performed using resources of the National Energy Research Scientific Computing Center, a DOE Office of Science User Facility supported by the Office of Science of the US Department of Energy under contract no.DE-AC02-05CH11231.

This manuscript has been authored by UT-Battelle, LLC under Contract No. DE-AC05-00OR22725 with the U.S. Department of Energy. The United States Government retains and the publisher, by accepting the article for publication, acknowledges that the United States Government retains a non-exclusive, paid-up, irrevocable, world-wide license to publish or reproduce the published form of this manuscript, or allow others to do so, for United States Government purposes. The Department of Energy will provide public access to these results of federally sponsored research in accordance with the DOE Public Access Plan (http://energy.gov/downloads/doe-public-access-plan).

[1] M. Lilienblum, T. Lottermoser, S. Manz, S. M. Selbach, A. Cano, and M. Fiebig, Nature Physics **11**, 1070 (2015).

[2] S. Lee, A. Pirogov, M. Kang, K.-H. Jang, M. Yonemura, T. Kamiyama, S.-W. Cheong, F. Gozzo, N. Shin, H. Kimura, Y. Noda, and J.-G. Park, Nature (London) **451**, 805 (2008).

[3] S. Seki, Y. Onose, and Y. Tokura, Physical Review Letters **101**, 067204 (2008).

[4] K. Kimura, H. Nakamura, K. Ohgushi, and T. Kimura, Physical Review B **78**, 140401(R) (2008).

[5] M. Frontzek, J. T. Haraldsen, A. Podlesnyak, M. Matsuda, A. D. Christianson, R. S. Fishman, A. S. Sefat, Y. Qiu, J. R. D. Copley, S. Barilo, S. V. Shiryaev, and G. Ehlers, Physical Review B **84**, 094448 (2011).

[6] M. Frontzek, G. Ehlers, A. Podlesnyak, H. Cao, M. Matsuda, O. Zaharko, N. Aliouane, S. Barilo, and S. V. Shiryaev, Journal of Physics: Condensed Matter **24**, 016004 (2012).

[7] K. Kimura, T. Otani, H. Nakamura, Y. Wakabayashi, and T. Kimura, Journal of the Physical Society of Japan **78**, 113710 (2009).

[8] A. B. Garg, A. K. Mishra, K. K. Pandey, and S. M. Sharma, Journal of Applied Physics **116**, 133514 (2014).

[9] M. Poienar, F. Damay, C. Martin, J. Robert, and S. Petit, Physical Review B **81**, 104411 (2010).

[10] M. Poienar, F. Damay, C. Martin, V. Hardy, A. Maignan, and G. Andre, Physical Review B **79**, 014412 (2009).

[11] M. Poienar, V. Hardy, B. Kundys, K. Singh, A. Maignan, F. Damay, and C. Martin, Journal of Solid State Chemistry **185**, 56 (2012).

[12] F. Wang and A. Vishwanath, Physical Review Letters **100**, 077201 (2008).

[13] T. Okuda, Y. Beppu, Y. Fujii, T. Onoe, N. Terada, and S. Miyasaka, Physical Review B **77**, 134423 (2008).

[14] T. Okuda, S. Oozono, T. Kihara, and M. Tokunaga, Journal of the Physical Society of Japan **82**, 014706 (2013).

[15] J. Fan, L. X. Feng, W. Y. Zhong, and H. J. Rong, Chin. Phys. B **21**, 077502 (2012).

[16] O. Aktas, K. D. Truong, T. Otani, G. Balakrishnan, M. J. Clouter, T. Kimura, and G. Quirion, Journal of Physics: Condensed Matter **24**, 036003 (2012).

[17] K. Kimura, H. Nakamura, S. Kimura, M. Hagiwara, and T. Kimura, Physical Review Letters **103**, 107201 (2009).

[18] H. Yamaguchi, S. Ohtomo, S. Kimura, M. Hagiwara, K. Kimura, T. Kimura, T. Okuda, and K. Kindo, Physical Review B **81**, 033104 (2010).

[19] S. Lin, K. Barros, E. Mun, J. Kim, M. Frontzek, S. Barilo, S. V. Shiryaev, V. S. Zapf, and C. D. Batista, Physical Review B **89**, 220405(R) (2014).

[20] E. Mun, M. Frontzek, A. Podlesnyak, G. Ehlers, S. Barilo, S. V. Shiryaev, and V. S. Zapf, Physical Review B **89**, 054411 (2014).

[21] T. Arima, Journal of the Physical Society of Japan **76**, 073702 (2007).

[22] F. Ye, Y. Ren, Q. Huang, J. A. Fernandez-Baca, P. Dai, J. W. Lynn, and T. Kimura, Physical Review B **73**, 220404(R) (2006).

[23] X. Fabréges, S. Petit, I. Mirebeau, S. Pailhés, L. Pinsard, A. Forget, M. T. Fernandez-Diaz, and F. Porcher, Physical Review Letters **103**, 067204 (2009).

[24] N. Terada, Y. Narumi, Y. Sawai, K. Katsumata, U. Staub, Y. Tanaka, A. Kikkawa, T. Fukui, K. Kindo, T. Yamamoto, R. Kanmuri, M. Hagiwara, H. Toyokawa, T. Ishikawa, and H. Kitamura, Physical Review B **75**, 224411 (2007).

[25] S. Toth, B. Wehinger, K. Rolfs, T. Birol, U. Stuhr, H. Takatsu, K. Kimura, T. Kimura, H. Ronnow, and C. Ruegg, Nature Communications **7**, 13547 (2016).

[26] K. Park, J. Oh, J. Leiner, J. Jeong, K. Rule, M. Le, and J.-G. Park, Physical Review B **94**, 104421 (2016).

[27] G. Quirion, M. J. Tagore, M. L. Plumer, and O. A. Petrenko, Physical Review B **77**, 094111 (2008).

[28] P. Sharma, J. Ahn, N. Hur, S. Park, S. Kim, S. Lee, J.-G. Park, S. Guha, and S.-W. Cheong, Physical Review Letters **93**, 177202 (2004).

[29] C. Chiorescu, J. Neumeier, and J. Cohn, Physical Review Letters **101**, 257202 (2008).

[30] L. Jiang, M. Zhang, and Q. Jiang, Journal of Applied Physics **104**, 083718 (2008).

[31] M. Stone, J. Niedziela, D. Abernathy, L. DeBeer-Schmitt, G. Ehlers, O. Garlea, G. Granroth, M. Graves-Brook, A. Kolesnikov, A. Podlesnyak, and B. Winn, Review of Scientific Instruments **85**, 045113 (2014).

[32] O. Arnold, J. C. Bilheux, J. M. Borreguero, A. Buts, S. I. Campbell, L. Chapon, M. Doucet, N. Draper, R. F. Leal, M. A. Gigg, V. E. Lynch, A. Markvardsen, D. J. Mikkelson, R. L. Mikkelson, R. Miller, K. Palmen, P. Parker, G. Passos, T. G. Perring, P. F. Peterson, S. Ren, M. A. Reuter, A. T. Savici, J. W. Taylor, R. J. Taylor, R. Tolchenov, W. Zhou, and J. Zikovsky, Nuclear Instruments and Methods in Physics Research Section A: Accelerators, Spectrometers, Detectors and Associated Equipment **764**, 156 (2014).

[33] D. Bansal, C. Li, A. Said, D. Abernathy, J.-Q. Yan, and O. Delaire, Physical Review B **92**, 214301 (2015).

[34] T. Toellner, A. Alatas, and A. Said, Journal of Synchrotron Radiation **18**, 605 (2011).

[35] A. Said, H. Sinn, and R. Divan, Journal of Synchrotron Radiation **18**, 492 (2011).

[36] S. Lovesey, *Theory of neutron scattering from condensed matter* (Clarendon Press, Oxford, 1984).

[37] A. Huq, J. P. Hodges, O. Gourdon, and L. Heroux, Z. Kristallogr. Proc. **1**, 127 (2011).

[38] A. C. Larson and R. B. Von Dreele, *GSAS General Structure Analysis System, Report LAUR 86-748* (Los Alamos National Laboratory, 1986).

[39] B. H. Toby, Journal of Applied Crystallography **34**, 210 (2001).

[40] R. V. Dreele, J. Jorgensen, and C. Windsor, J. Appl. Cryst. **15**, 581 (1982).

[41] H. Kadowaki, H. Kikuchi, and Y. Ajiro, Journal of Physics: Condensed Matter **2**, 4485 (1990).

[42] G. Kresse and J. Hafner, Physical Review B **47**, 558 (1993).

[43] G. Kresse and J. Furthmüller, Physical Review B **54**, 11169 (1996).

[44] G. Kresse and J. Furthmüller, Computational Materials Science **6**, 15 (1996).

[45] J. Perdew, K. Burke, and M. Ernzerhof, Physical Review Letters **77**, 3865 (1996).

[46] S. Dudarev, G. Botton, S. Savrasov, C. Humphreys, and A. Sutton, Physical Review B **57**, 1505 (1998).
[47] I. I. Mazin, Physical Review B **75**, 094407 (2007).
[48] E. J. Kan, H. J. Xiang, Y. Zhang, C. Lee, and M.-H. Whangbo, Physical Review B **80**, 104417 (2009).
[49] A. A. Togo, F. Oba, and I. Tanaka, Physical Review B **78**, 134106 (2008).
[50] G. Squires, *Introduction to the theory of thermal neutron scattering* (Cambridge University Press, 1978).
[51] J. Li, A. Sleight, C. Jones, and B. Toby, Journal of Solid State Chemistry **178**, 285 (2005).
[52] B. Klobes, M. Herlitschke, K. Rushchanskii, H.-C. Wille, T. Lummen, P. van Loosdrecht, A. Nugroho, and R. Hermann, Physical Review B **92**, 014304 (2015).
[53] C. Liu and D. Morelli, Journal of Electronic Materials **40**, 678 (2011).
[54] P. Klemens, *Solid State Physics: Advances in Research and Applications – Thermal Conductivity and Lattice Vibrational Modes* (Vol. 7, Academic Press Inc., New York, 1958).
[55] T. Tritt, *Thermal Conductivity: Theory, Properties, and Applications* (Kluwer Academic/Plenum Publishers, New York, 2004).
[56] O. Aktas, G. Quirion, T. Otani, and T. Kimura, Physical Review B **88**, 224104 (2013).
[57] X. Wang, C. Fan, Z. Zhao, W. Tao, X. Liu, W. Ke, X. Zhao, and X. Sun, Physical Review B **82**, 094405 (2010).